Pergamon

Int. J. Heat Mass Transfer. Vol. 37, No. 12, pp. 1759–1771, 1994

0017-9310/94 $7.00+0.00

0017-9310(93)E0123-X

Measurement of wall conductive heat flux in turbulent gas flow by laser beam deflection

F. EL AMMOURI and J. TAINE

Laboratoire EM2C, UPR 288 du CNRS et de l'ECP, Ecole Centrale Paris,
92295 Châtenay-Malabry Cedex, France

(*Received in final form* 22 *November* 1993)

Abstract—The wall conductive flux in gas for a turbulent and homogeneous flow in a channel is directly deduced from a laser beam deflection technique. The main advantage of this method is the elimination of the radiative flux contribution. The beam deflection is due to the refractive index gradient field induced by a temperature gradient field at constant pressure. Experimental data are treated by using a parameter estimation method. Experimental fluxes associated with Reynolds number based on the hydraulic diameter in the range $1.75 \times 10^4 - 3.5 \times 10^4$ and a temperature gradient in the range 60–120 K mm^{-1} agree with the results of a two-dimensional turbulence model when taking into account all uncertainty causes.

1. INTRODUCTION

TWO KINDS of techniques are used to measure directly or indirectly the temperature field or wall conductive heat flux in gases: optical methods [1] and intrusive methods.

Among the intrusive techniques hot wires, generally 2.5 μm thick, and thermocouples, about 50 μm thick, are often used [2–5]. Each kind of probe is an opaque body for which the thermal balance depends on the emitted and absorbed radiative fluxes in the medium considered. If the gas is transparent, air for example, the incident flux on the probe issues from different wall elements which may be much hotter or cooler than the probe. Even if the convective heat transfer coefficient is large in the case of flow around a fine wire, the radiation effect cannot be neglected near the wall, where the fluid velocity is low [6]. On the other hand, the intrusive techniques considered are often used with temperature difference between the wall and the gas of about 15 K [7–10]. Radiation effects are therefore weak. But here we consider a temperature difference of about 150 K.

Optical techniques possess the considerable advantage of not disturbing the gas hydrodynamical properties where the measurements occur. They generate practically no inertial errors so that rapidly changing processes can be accurately followed, provided that the processing method is characterized by a sufficiently high sampling frequency. Depending on the kind of interaction between the radiation and the gas we can distinguish, for example: (i) spectroscopic methods such as the two-line absorption technique [11] or inversion of gas absorption line shape for laminar [6] or turbulent [12] gas flow; (ii) Rayleigh [13], Raman [14] and coherent anti-Stokes–Raman [15] scattering methods; and (iii) methods based on properties depending on the optical refraction index such as interferential [16] and holographic [17] techniques, shadow and Schlieren [18] methods. A variant of this method is the laser beam deflection technique. Previous authors have used this method to measure gas density in molecular free jets [19], thermal diffusivity for material [20], photothermal spectroscopy [21, 22] or gas temperature in a laminar free convection [23].

In this paper we extend the laser beam deflection technique in order to determine the wall conductive heat flux in a turbulent air flow. It is worth noticing that this method is interesting when the wall radiative flux is not negligible and especially when radiation and convection are coupled. The major difficulty is that the turbulent conductive sublayer is small compared to the laser beam radius of about 0.5 mm. The optical set-up is based on an He–Ne gas laser and a very precise photodiode position sensor. The laser beam displacements induced by the refraction index variations due to a non-uniform temperature in an homogeneous medium are recorded for different inlet laser beam positions. Experimental data are treated by using a parameter estimation method which leads to an analytical temperature distribution. The principle of measurements and the data treatment are given in Section 2. The EM2C wind channel, previously studied elsewhere [24, 25], is briefly described in Section 3.1, the optical and experimental procedures in Sections 3.2 and 3.3. Section 4 is related to the experimental results and their accuracy. A comparison between these results and those of a two-dimensional (2D) four supplementary turbulence model [26, 27], briefly described in the Appendix, is made in the last section. This comparison takes into account both the limitations of the 2D turbulence model and the uncertainties related to the inlet gas flow data and the temperature fields in the EM2C wind channel.

NOMENCLATURE

a	thermal diffusivity
A	parameter vector
c_p	specific heat at constant pressure
D	displacement on the photodiode sensor
Dh	hydraulic diameter
E	height of the channel
h	convective transfer coefficient
H	enthalpy
k	turbulent kinetic energy
$\dot{m}$	mass flow rate
M	number of experimental data
n	index of refraction
N	number of parameters
p	pressure
Pr	Prandtl number
$\mathbf{r}$	positon vector
R	curvature radius
Re	Reynolds number
s	simplex edge size
T	temperature
u	axial velocity
$\mathbf{u}$	inner normal unit vector
v	transverse velocity
x	axial distance from the inlet of the channel
y	normal distance to the upper horizontal wall
z	direction of the laser beam.

Greek symbols

β	Gladstone–Dale constant
θ	$\overline{T'^2}/2$
ϕ	wall conductive heat flux
δ	uncertainty on y
ε	dissipation rate of k
ε_θ	dissipation rate of θ
λ	thermal conductivity
μ	viscosity
ρ	density
σ	objective function.

Subscripts

1	related to section 1
2	related to section 2
a	related to the inlet of the channel
b	bulk
d	related to the displacement of the laser beam
l	related to the lower wall
m	related to the model of turbulence
t	turbulent quantity
u	related to the upper wall.

Superscripts

A'	fluctuating part of A
A^{++} and A^{+}	dimensionless expression of A
$\bar{A}$	Reynolds averaging
$\tilde{A}$	Favre averaging, $\tilde{A} = \overline{\rho A}/\bar{\rho}$.

2. PRINCIPLES OF MEASUREMENT AND TREATMENT

A light beam crossing a medium of nonhomogeneous refractive index $n(\mathbf{r})$ is deflected toward the stronger n value region. The differential equation describing the trajectory of the light beam is [28]

$$\frac{1}{R(\mathbf{r})} = \frac{1}{n(\mathbf{r})}\mathbf{grad}\,[n(\mathbf{r})]\cdot\mathbf{u}, \tag{1}$$

where $R(\mathbf{r})$ is the curvature radius at point $\mathbf{r}$ and $\mathbf{u}$ is the inner normal unit vector. For pure gases at constant pressure p the refractive index is given as a function of temperature by the Gladstone–Dale law [28]

$$n = 1 + \frac{K}{T} \quad \text{with} \quad K = \beta\frac{pT_s}{p_s}, \tag{2}$$

where T_s and p_s are the standard temperature and pressure, respectively ($T_s = 273.15$ K, $p_s = 1$ atm), β is the Gladstone–Dale constant which depends only on the gas nature and the light beam wavelength λ. In the considered case of air and for a wavelength λ of 0.6328 μm (the He–Ne laser wavelength), β is equal to 2.920×10^{-4}. Equations (1) and (2) show that the light beam trajectory clearly depends on the temperature distribution of the crossed homogeneous gaseous medium at constant pressure, so we can expect to determine the medium temperature field using a set of well-chosen beam trajectories. We consider in fact a 1D temperature profile $T(y)$ which varies only in the direction Oy orthogonal to the laser propagation direction Oz (Fig. 1). Equation (1) becomes

$$\frac{y''}{1+y'^2} = \frac{1}{n}\frac{\mathrm{d}n}{\mathrm{d}y}. \tag{3}$$

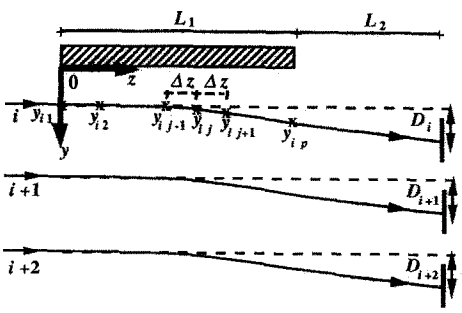

FIG. 1. Principle view of laser beam deviation and displacement; definition of axes and geometry.

where y' and y'' are the first and second derivatives of y vs z, respectively. For air, n is practically equal to 1 and y' negligible compared to 1. We therefore obtain

$$y'' = -\frac{K}{T^2}\frac{\mathrm{d}T}{\mathrm{d}y}. \tag{4}$$

In turbulent flows, the local gas temperature field can be written:

$$T = \bar{T} + T', \tag{5}$$

where $\bar{T}$ and T' are the mean and fluctuating parts of T, respectively. A second-order Taylor expansion is applied to the term $1/T^2$ of equation (4) and we obtain

$$y'' = -\frac{K}{\bar{T}^2}\left[\frac{\mathrm{d}\bar{T}}{\mathrm{d}y} + \frac{\mathrm{d}T'}{\mathrm{d}y} - 2\frac{T'}{\bar{T}}\frac{\mathrm{d}\bar{T}}{\mathrm{d}y} - \frac{1}{\bar{T}}\frac{\mathrm{d}\overline{T'^2}}{\mathrm{d}y} + 3\frac{T'^2}{\bar{T}^2}\frac{\mathrm{d}\bar{T}}{\mathrm{d}y}\right]. \tag{6}$$

Time averaging of this equation leads to

$$\overline{y''} = -\frac{K}{\bar{T}^2}\left[\frac{\mathrm{d}\bar{T}}{\mathrm{d}y} - \frac{1}{\bar{T}}\frac{\mathrm{d}\overline{T'^2}}{dy} + 3\frac{\overline{T'^2}}{\bar{T}^2}\frac{\mathrm{d}\bar{T}}{\mathrm{d}y}\right]. \tag{7}$$

To evaluate the order of magnitude of the last two terms of the last factor in equation (7), called B, compared to the first term, called A, we use a four supplementary equations turbulence model [26, 27] which is given in the Appendix. As it is shown in Fig. 2, B is negligible compared to A. The absolute value of the ratio B/A is always less than 1.5×10^{-2} in our experimental conditions. Equation (7) becomes

$$\overline{y''} = -\frac{K}{\bar{T}^2}\frac{\mathrm{d}\bar{T}}{\mathrm{d}y} \tag{8}$$

or in a discretized form (see Fig. 1)

$$y_{ij+1} = 2y_{ij} - y_{ij-1} - \frac{K}{\bar{T}_{ij}^2}\left(\frac{\mathrm{d}\bar{T}}{\mathrm{d}y}\right)_{ij}\Delta z^2, \tag{9}$$

where y_{ij} is the distance to the wall of a discretized point j of the trajectory i, Δz is the spatial increment in the laser direction. The refractive index gradient is assumed to be uniform between y_{ij-1} and y_{ij+1}. The displacements D_i are measured on a sensor at a given distance L_2 from the channel for a great number of entrance distances y_{i1} from the wall. The expression of the time averaged displacements is then given by

$$\bar{D}_i = y_{ip} - y_{i1} + y'_{ip}L_2, \tag{10}$$

where y_{ip} and y'_{ip} are related to the exit point of the trajectory in the channel. The laser beam is, in practice, maintained parallel to the wall and displaced vertically from a position very closed to the wall to a position where the temperature gradient becomes too small to be detected. Thus, we obtain a set of experimental couples $(y_{i1}, \bar{D}_i)$. Our objective is to determine the wall conductive flux in the gas using the set of experimental displacements. In a previous paper [23] two different methods have been used to treat the experimental data:

1. The parabolical trajectory (PT) method assumes that each light beam crosses a path characterized by a constant refractive index gradient. This assumption leads to a parabolical beam trajectory. However, in a forced turbulent non-isothermal flow a strong temperature gradient appears near the wall. Consequently the refractive index gradient seen by a beam is not uniform and the PT method is not valid.

2. In fact we use the parameter estimation (PE) method in which the temperature field near the wall is expressed as a given function depending on a few parameters. A sequential simplex search [29] can be employed to optimize these parameters. For M couples of measurements $(y_{i1}, \bar{D}_i)$ we choose a dimensionless temperature function T^+

$$T^+ = \frac{T_u - \bar{T}}{T_u - T_l} = g(y^+, a_1, a_2, \ldots, a_N), \tag{11}$$

where T_u and T_l are the upper and the lower wall temperatures, respectively. The function g depends on N parameters a_j $(j = 1, 2, \ldots, N)$ to be determined and on the dimensionless distance to the wall y^+ defined by

$$y^+ = \frac{y}{E}, \tag{12}$$

where E is the height of the channel. The number of parameters N is smaller than the number M of experimental couples $(y_{i1}, \bar{D}_i)$. The approach of Spendly *et al.* [30] is used to determine the temperature function parameters. For each step of this method the two main quantities are the parameter vector $A(a_1, a_2, \ldots, a_N)$ called the simplex vertex and the objective function σ to be minimized, defined by

$$\sigma = \sqrt{\frac{1}{M}\sum_{i=1}^{M}(D_i - \bar{D}_i)^2}, \tag{13}$$

where D_i $(i = 1, 2, \ldots, M)$ is the displacement in condition i, calculated by using the parameter vector A, the temperature function g and the basic equations (1)–(10). For a problem with N parameters to be

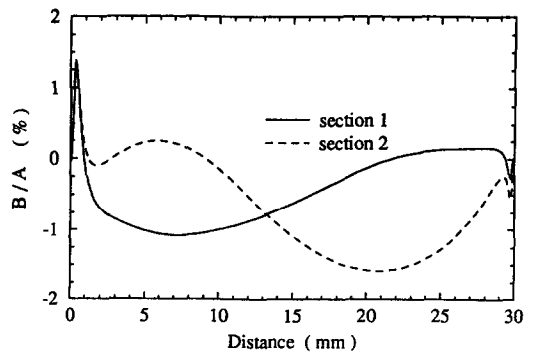

FIG. 2. Evolution of the ratio B/A at sections 1 and 2 versus the distance y to the upper wall, case of experiment E5 (see Section 4).

determined, an initial vector A_0 is chosen and N others are determined using the expression

$$A_k = A_0 + (a_{k1}, a_{k2}, \ldots, a_{kN}), \quad k = 1, 2, \ldots, N$$
$$a_{kl} = p\delta_{kl} + q(1 - \delta_{kl}), \tag{14}$$

where δ_{kl} designates the Kronecker symbol; p and q are given by

$$p = \frac{s}{N\sqrt{2}}(\sqrt{N+1} + N - 1)$$
$$q = \frac{s}{N\sqrt{2}}(\sqrt{N+1} - 1), \tag{15}$$

where s is the simplex edge size. Corresponding to these $N+1$ parameter vectors A_k, $N+1$ objective function σ_k values are evaluated. The vertex at which σ is worst is rejected and replaced by a new vertex obtained from the other N vertices [29, 30]. A new value of the objective function is calculated at this new vertex and compared with the $N+1$ previous objective functions. The procedure is repeated until one of the following two criteria is satisfied:

(i) A physical convergence is obtained when

$$\sigma < \varepsilon_\sigma D_{\max}, \tag{16}$$

where ε_σ is the estimated variance of the experimental relative error on the displacement (to be determined in Section 4) and $D_{\max}$ is the maximum displacement. The physical uncertainty on the obtained value of A associated to σ will also be discussed in Section 4.

(ii) No subsequent adjustment of A would lead to further improvement. The criterion of no further improvement can be expressed as

$$\sqrt{\frac{1}{N+1}\sum_{k=1}^{N+1}(\sigma_k - \langle\sigma\rangle)^2} < \varepsilon\langle\sigma\rangle, \tag{17}$$

with

$$\langle\sigma\rangle = \frac{1}{N+1}\sum_{k=1}^{N+1}\sigma_k, \tag{18}$$

where ε is an arbitrary small value. This is a criterion of mathematical significance: the average of the last $N+1$ parameter vectors is then considered as a new A_0 vector and the whole procedure is restarted with a smaller simplex size s. The method is applied until the physical convergence criterion [equation (16)] is reached. If the function g defined by equation (11) is polynomial vs y^+

$$T^+ = a_1 y^+ + a_2 y^{+2} + \ldots + a_N y^{+N} \tag{19}$$

then the coefficient a_1 leads to the wall conductive flux value.

3. EXPERIMENTAL SET-UP AND PROCEDURE

3.1. *The EM2C wind channel*

The EM2C wind channel has been previously studied elsewhere [6, 24, 25] and consequently only a brief description is given here. Heated air at about 393 K flows inside a horizontal wind channel with a rectangular cross-section (0.15 m wide, 0.03 m high and 2 m long) following a nozzle. The upper and lower walls of the channel were maintained at constant but different temperatures. The upper wall is heated electrically and was stabilized in our experiments at a temperature T_u of about 530 K; the lower one T_l was held at about 373 K using a liquid–vapour water phase change. Deviations from the fixed wall temperatures were given by 25 chromel–alumel thermocouples. The maximum deviations are about ± 5 K for T_l and ± 15 K for T_u. The channel end was open to the atmosphere, all the studied flows were then at atmospheric pressure which was measured during each experiment. A simple control thermocouple, without radiation shield, gives the mean air temperature T_a at the entrance $x = 0$ of the wind channel.

Two sets of four windows located at $x = 0.5$ m and at $x = 1.7$ m of the inlet section of the channel enable optical measurements at two cross-sections of the channel 1.2 m away from each other (Fig. 3a). At each side of a section a sapphire (Al_2O_3) slab, 3 mm thick and 40 mm of diameter, brazed on a titanium ring was put in line with the inside vertical surface of the channel to a tolerance of 0.1 mm in order to avoid flow pertubations. This sapphire slab and a fluoride CaF_2 slab of the same size delimit a vacuum tight enclosure in order to avoid laser beam deviation due to natural convection (Figs. 3a, b). The laser beam deviation technique described in the previous section was applied at the two optical sections.

Gas temperature measurements were also made by two movable thermocouples (chromel–alumel, 0.25 mm diameter) equipped with radiation shields, located 3 cm away from the optical sections of the channel. Thermocouples were displaced in the flow by micrometric screws and the radiation shields were retracted in the upper wall of the channel before proceeding to optical measurements (Figs. 3b, c). The thermocouple measurements were not valid for distances to the wall y of less than 4 mm because of the perturbations generated by the recirculating flow induced by the hole in the wall, and also because of the effect of direct radiation from the hot wall on the thermocouple (Fig. 3c). In the case of the turbulent flow considered, we consider that the temperature measured by the thermocouple in the inner region of the channel (4 mm away from each wall) is close to the gas temperature with an error of 1–2 K. In fact, an estimated value of the convection coefficient in the flow core at the thermocouple junction point is about 500 W m^{-2} K^{-1}, while a crude estimation of an effective radiative transfer coefficient at the same point is about 5 W m^{-2} K^{-1}. Temperature measurements by both techniques (beam deflection and thermocouple) at the upstream section 1 are used as inlet conditions in flow calculations; results of these calculations are then compared to measurements at the downstream section 2 in Section 5.

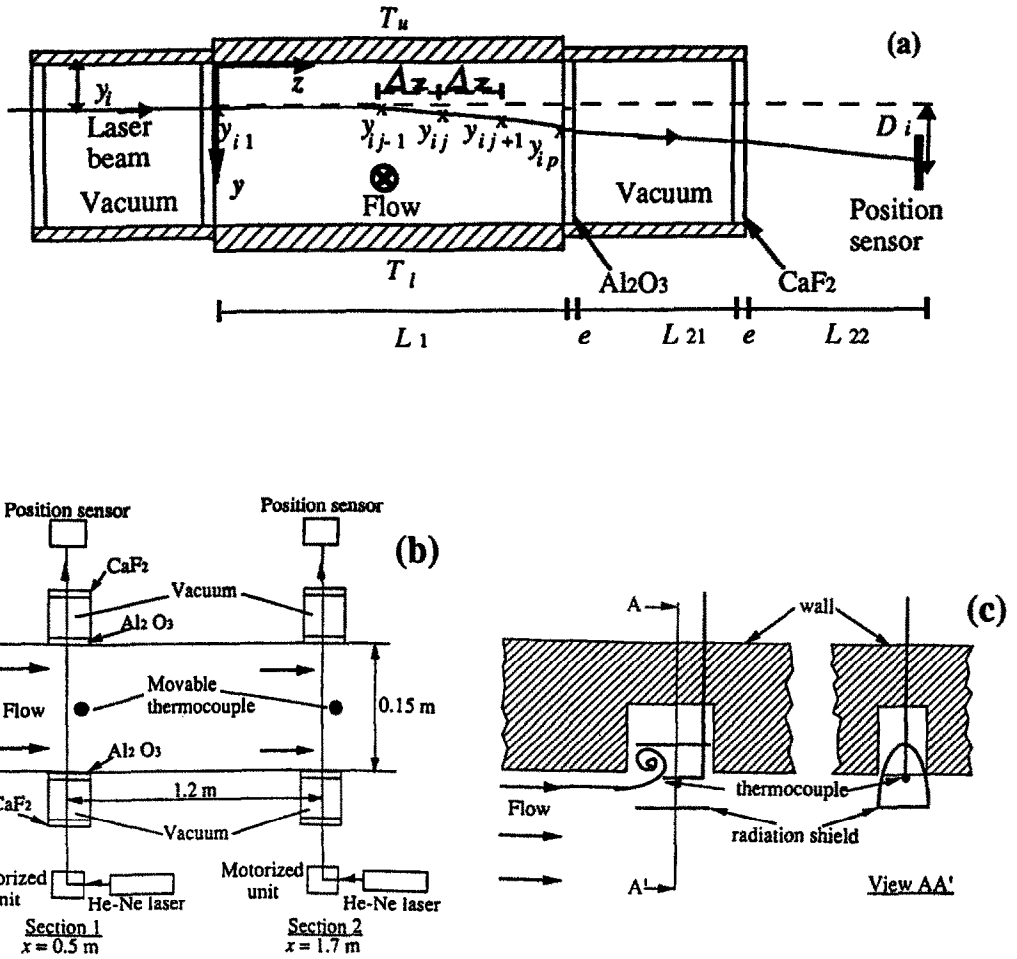

FIG. 3. Optical set-up and general description: (a) trajectory of the laser beam in a sectional view of the channel, (b) general view for He–Ne laser displacements measurements, and (c) recirculating flow near the thermocouple with radiation shields.

3.2. *Optical setup*

Figure 3 shows the optical arrangement for displacement measurements. The light sources were two Spectra-Physics He–Ne lasers of 0.95 mW used in the Gaussian mode TEM00. Two motorized units including "Microcontrol" step-by-step motors and focusing lenses allowed precise vertical displacements of the beams, parallel to the horizontal walls, and permitted displacement measurements at any position with a spatial resolution of about 10 μm. The beams were focused in the middle of the channel in order to minimize their sizes. They were deflected toward the colder wall and were collected by two "SDC" photodiode position sensors (type SD-386-22-21-251) characterized by an active surface of 10×10 mm^2 and a response time less than 10^{-6}s. With the chosen electronic devices beam displacements were acquired with a frequency as high as 30 kHz. The laser spot diameter on the position sensor due to natural expansion was about 5–6 mm. Each position sensor was displaced by the step-by-step motor in such a manner that the laser spot was always in the sensor centre region, to get optimal response linearity. Any displacement of the laser spot centre was converted into an electric tension. The conversion coefficient tension/displacement was 2.45 ± 0.02 V mm^{-1} for the first sensor and 2.67 ± 0.02 V mm^{-1} for the second. These values were valid only if the centre of the laser spot was inside a 4-mm diameter circular region of the position sensor. In fact, the sensor was moved to follow the laser spot. This pursuit procedure was repeated again. After two movements, the total displacement of the laser spot was determined by the sum of the imposed displacements of the sensor and the displacement on the sensor which was determined from the measured tension. All the movements of the step-by-step motors were controlled by a personal computer (Commodore 286) which also performed the acquisition of the laser spot displacements.

The laser beam size and the distance between the heated surface and the laser beam axis were difficult to determine. The beam size was estimated by the following procedure without heating the channel: first the laser beam is moved until it just disappears behind

the wall, and in a second step to appear parallel to this wall, with a similar diffraction figure. The diameter of a laser beam is estimated by the measurement of the beam displacement $\phi_1 = 1.1 \pm 0.1$ mm, for section 1; $\phi_1 = 0.9 \pm 0.1$ mm, for section 2. The second previously considered position of the beam is taken as a reference at the distance $y_{i1} = \phi_i/2$ to the wall for the determination of a current distance y_i by the procedure described above. Consequently the uncertainty on a current distance to the wall y_i is in practice due to the uncertainty on the laser beam diameter of about ± 0.1 mm.

3.3. *Experimental procedure*

In turbulent flows, the laser beam displacement is time dependent because of temperature fluctuations. The displacement D_i is averaged during a period of time Δt and with a sampling frequency f. Δt is chosen to be long enough (from 1 to 3 s) to ensure that $\bar{D}_i$ is time independent (standard deviation from the averaged displacement less than the experimental noise) and f is taken greater than the double of the highest frequency observed in the spectral analysis of displacement $D_i(t)$, in practice from 5 to 15 kHz. Thus, we obtain a set of couples $(y_{i1}, \bar{D}_i)$.

It is worth noticing that in an experiment without heating a displacement up to a few 0.1 mm on the photodiode sensor can appear. This displacement is due to three factors:

(i) The photodiode sensor surface receives, in addition to the main laser beam, many other small beams due to unavoidable multiple reflections between the different optical interfaces crossed by the laser beam. Their effect is to modify the tension issued from the position sensor which is related to the barycentre of the beams weighted by their intensities.

(ii) The step-by-step system generates an uncertainty of about 10 μm on y_i and about $\pm 5 \times 10^{-5}$ rad on the beam incidence angle at the entrance in the channel which corresponds to a displacement of ± 0.11 mm at a distance of 2 m (the distance between the step-by-step motor displacing the laser beam and the position sensor).

(iii) The different optical slabs crossed by the laser beam are not rigorously parallel. The result is a displacement of the beam on the photodiode surface.

The displacements observed in our experimental conditions must be corrected if we take into account the three previous error causes. For this purpose we use displacements issued from an experiment with heating but without air flow. As the upper wall is warmer than the lower one, a stratification régime is observed and natural convection does not appear. Therefore we consider that the temperature field in the gas is purely conductive but nonlinear. The theoretical displacement deduced from the temperature field can be numerically calculated using the finite difference method applied to equation (8). The difference between the theoretical and experimental displacements obtained with heating but without flow is used to correct the experimental displacements for our experiments.

Another source of error could be the effect of gas temperature variation inside a laser beam section. In the turbulent non-isothermal flow considered here, the temperature variation near the wall is about 100 K inside the section of the laser beam. We have calculated the deformation of the beam generated by this temperature variation. In fact the laser beam is divided into many elementary beams. Their sections are assumed to be isothermal. The global displacement D_{cg} is related to the barycentre of these beams weighted by their intensities on the photodiode surface. The highest relative difference between D_{cg} and the displacement of the beam centre D_{mc} is about 2×10^{-2}. This effect induces a variation in the wall conductive flux of about $\pm 1 \times 10^{-2}$.

We have also studied the effect of the lateral thermal boundary layers on the deviation of the laser beam. Figure 10 shows an example of the comparison between the gas temperature field in the middle of the wind channel section and the assumed linear temperature field of the lateral wall vs the vertical distance y. The difference between the two fields explains the presence of thermal boundary layers near the vertical walls. We

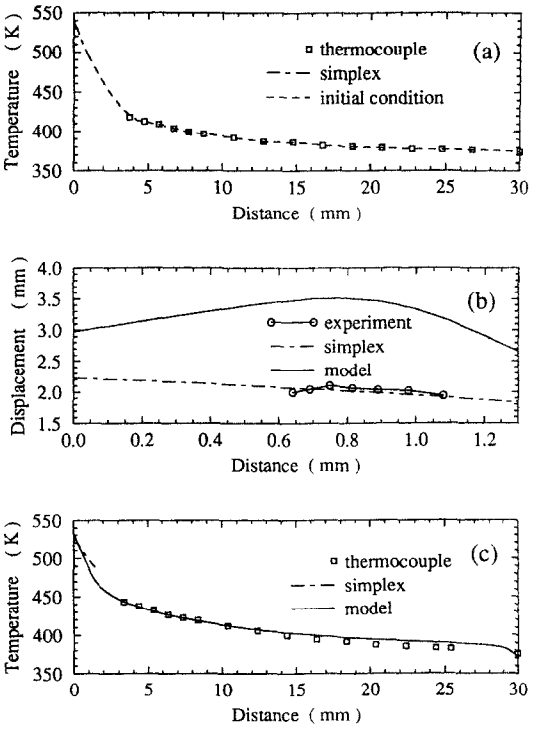

FIG. 4. Results of experiment E1: (a) gas temperature fields vs the distance y at section 1. The initial condition profile is the temperature field which allows to start the model used in Section 5. The simplex profile is the temperature field deduced from the PE method, (b) displacement fields vs the distance y at section 2, and, (c) gas temperature fields vs the distance y at section 2.

have assumed that these boundary layers near the vertical walls have the same dimensionless temperature field than the one found in the boundary layer near the upper wall. The maximum relative difference between the displacements computed with and without taking into account the lateral boundary layers is 3×10^{-2}. This difference induces a maximum relative difference between the corresponding wall fluxes of about 1×10^{-2}.

Consequently these two effects are neglected in all the treatment of the experiments.

4. EXPERIMENTAL RESULTS

Experiments have been carried out for five different values of the inlet Reynolds number based on the hydraulic diameter $Re_{Dh}(x = 0)$ varying between 10^4 and 3.5×10^4. All experimental conditions, i.e. the Reynolds number $Re_{Dh}(x = 0)$, the upper and lower wall temperatures T_u and T_l, the approximate inlet air temperature T_a at $x = 0$, the mass flow rate and the experimental results, i.e. the wall temperature gradient and the wall conductive flux ϕ_{2d} with their uncertainties, which are discussed later, are summarized in Table 1. The PE method has been used to treat the laser beam displacement fields. In order to minimize computing time the first vector A_0 which serves to initialize the simplex search is chosen from a fit of the temperature field given by the 2D turbulence model in the conditions of the experiment. It should be noticed that the local wall temperature value at section 1 or 2 is fixed in all the treatment of the experiments.

As the laser beam deviation technique is not sensitive to a small temperature gradient, only the displacements D_i which are in the region defined by $0 < y < 1.1$ mm are treated by the PE method. In fact, the smallest distance of the beam y_{11} to the upper wall is fixed by the laser beam radius which is equal to 0.45 ± 0.1 mm at section 2. This value corresponds to a dimensionless distance y^{++}, classically defined from the friction velocity u_τ and the thermal gas diffusivity a at the wall temperature by

$$y^{++} = \frac{y u_\tau}{a} \tag{20}$$

equal to 7.5 ± 1.7 in the conditions of experiment E3, for example. Consequently no experimental displacement measurements can be achieved in the conductive sublayer defined by $0 < y^{++} < 3$–5. The other limiting value related to $y = 1.1$ mm corresponds to about $y^{++} = 20$.

Two approaches can be used to choose the temperature polynomial function g whose parameters are to be determined by the PE method:

(i) Only one function is applied to the region $0 < y < 1.1$ mm.

(ii) We assume that the temperature field is linear in the region $0 < y^{++} < y_L^{++}$ and polynomial in the region $y_L^{++} < y^{++} < 20$. At the limit between these two regions y_L, we ensure the continuity of T and dT/dy.

The convergence criterion $\varepsilon_\sigma D_{\max}$, defined by equation (16), has been taken to be equal to 0.1 mm. This value corresponds to the largest causes of uncertainty which are related, as seen in Section 3.2, to both the measurement of the distance y_i to the upper wall and to the uncertainty on the stability of the time averaged displacement $\bar{D}_i$.

The first approach has been successfully applied to experiments E1–E4 corresponding to Re_{Dh} up to 3×10^4 with different polynomial orders n from 2 to 6. A typical study of the sensitivity of the results to the uncertainty δ (in mm) to the measured value of the distance y_i to the wall has been carried out and the results given in Table 2. It leads to an uncertainty on the temperature gradient of about 6% in these conditions. On the other hand, the sensitivity to the coefficient a_1 of the linear term of equation (19), which is proportional to ϕ_{2d}, has been studied. After convergence, the results obtained for experiment E2 are summarized in Table 2 where σ_{+5}, σ_{-5}, σ_{+10} and σ_{-10}, denote the objective functions calculated for the imposed values of a_1 corresponding to the wall conductive fluxes $1.05\phi_{2d}$, $0.95\phi_{2d}$, $1.10\phi_{2d}$, and $0.90\phi_{2d}$, respectively. It appears that the simplex convergence is relatively sharp for a given value of δ. But the quite large uncertainties obtained around the centre value of ϕ_{2d} result from the variation range of δ and from the lack of experimental data in the conductive sublayer.

The PE method does not lead to convergence for

Table 1. Experimental conditions

Experiment	$Re_{Dh}(x = 0)$	T_u [K]	T_l [K]	T_a [K]	$\dot{m}$ [g s^{-1}]	$(dT/dy)_{2d}$ [K mm^{-1}]	ϕ_{2d} [kW m^{-2}]
E1	10 700	532±15	372±5	395±2	18.4±0.2	31.4± 1.4	1.35±0.06
E2	17 500	531±15	375±5	394±2	30.0±0.3	63.0± 3.7	2.71±0.16
E3	25 200	528±15	374±5	388±2	43.1±0.4	69.3± 9.1	2.98±0.39
E4	30 600	528±15	373±5	395±2	52.3±0.5	93.5± 3.8	4.02±0.16
E5	35 500	528±15	373±5	397±2	60.7±0.6	115.1±16.3	4.95±0.70

$Re_{Dh}(x = 0)$ is inlet Reynolds number based on the hydraulic diameter, T_u and T_l are the temperature of the upper and the lower wall, respectively, and T_a is the approximate temperature of air at the inlet of the channel; $\dot{m}$ is the mass flow rate; $(dT/dy)_{2d}$ the temperature gradient at the upper wall; ϕ_{2d} the wall conductive flux at section 2, obtained after convergence of the PE method.

Table 2. Results of experiment E2

n	δ [mm]	σ [mm]	σ_{+5} [mm]	σ_{-5} [mm]	σ_{+10} [mm]	σ_{-10} [mm]	$(dT/dy)_{2d}$ [K mm^{-1}]	ϕ_{2d} [kW m^{-2}]
2	−0.1	0.09	0.18	0.21	0.32	0.34	59.2	2.55
2	0	0.05	0.18	0.19	0.33	0.34	63.1	2.71
2	+0.1	0.03	0.18	0.18	0.35	0.35	66.7	2.87

n is the polynomial order of the temperature function used in the PE method; δ is the uncertainty on the distance y to the upper wall; $\sigma, \sigma_{+5}, \sigma_{-5}, \sigma_{+10}$ and σ_{-10} are objective functions related to ϕ_{2d}, $1.05\phi_{2d}$, $0.95\phi_{2d}$, $1.10\phi_{2d}$ and $0.90\phi_{2d}$, respectively

Table 3. Results of experiment E5

n	y_L [mm]	y_L^{++}	δ [mm]	σ [mm]	σ_{+5} [mm]	σ_{-5} [mm]	σ_{+10} [mm]	σ_{-10} [mm]	$(dT/dy)_{2d}$ [K mm^{-1}]	ϕ_{2d} [kW m^{-2}]
3	0.04	1	+0.1	0.06	0.41	0.38	0.81	0.71	131.3	5.65
5	0.08	2	+0.1	0.07	0.26	0.25	0.49	0.46	104.3	4.48
4	0.12	3	+0.1	0.10	0.46	0.44	0.90	0.78	121.8	5.24

y_L is the distance over which the temperature field is assumed to be linear and y_L^{++} is the corresponding dimensionless value.

experiment E5 when using the first approach. In this case the closest experimental point to the upper wall is located at y^{++} equal to 11, which is far away from the conductive sublayer limited by y^{++} equal to 3–5. Thus, the second approach is used to treat this experiment. The results obtained are summarized in Table 3. On the other hand, we have applied the second approach to experiments E1–E4. The wall conductive flux values obtained from this approach are the same as in the first one but with larger uncertainty ranges. Figures 4(b)–8(b), which are related to experiments E1–E5, respectively, show the evolution of the displacement fields at section 2 vs the distance y to the upper wall. As it is observed on these figures the displacement fields deduced from the PE method are close to the experimental ones. In Figs. 4(c)–8(c) the temperature fields at section 2 from the PE method and the thermocouple are represented vs the distance y while in Figs. 4(a)–8(a) temperature fields at section 1 are shown.

In Fig. 9 the standard deviation on the displacement D_i in the sections 1 and 2 are represented in the case of experiment E3 vs the distance y. We observe that this standard deviation reaches its maximum for y^{++} close to 15 and this property is valid for all the experiments. It can probably be related to a function of the dissipation rate ε_θ of the temperature variance. It is the aim of a future study.

5. COMPARISON WITH A 2D TURBULENCE MODEL AND DISCUSSION

As a 3D turbulence model is not available to us, the results obtained with a 2D turbulence model briefly described in the Appendix are compared with the experimental ones. The turbulence calculation at the section $x = 0$ is started with mechanically fully developed fields for u, k, ε and uniform fields for T, θ, ε_θ [T is equal to T_a in this first step, θ is taken equal to the very low value 10^{-5} K^2 while ε_θ is equal to $(\theta\varepsilon)/(0.45k)$]. In fact, the value of T_a given by the control thermocouple without radiation shield is only used in order to initialize the calculation; the air temperature field is thus replaced by the temperature field at section 1 deduced from the laser beam deflection

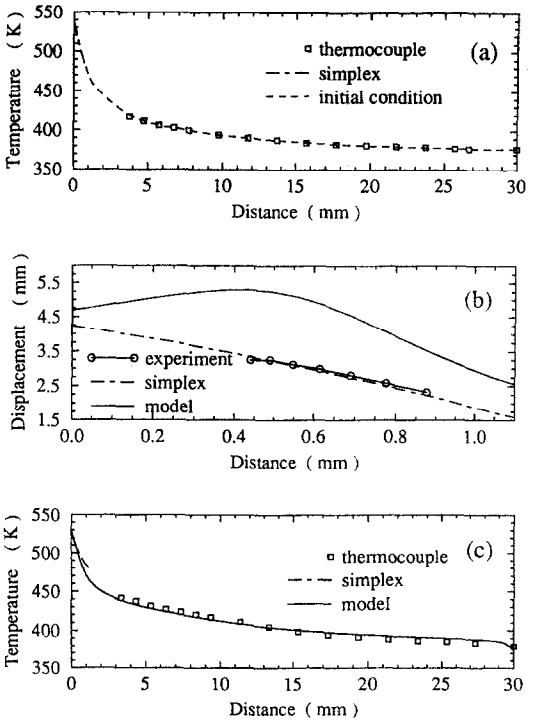

FIG. 5. Results of experiment E2. The legend is the same as Fig. 4.

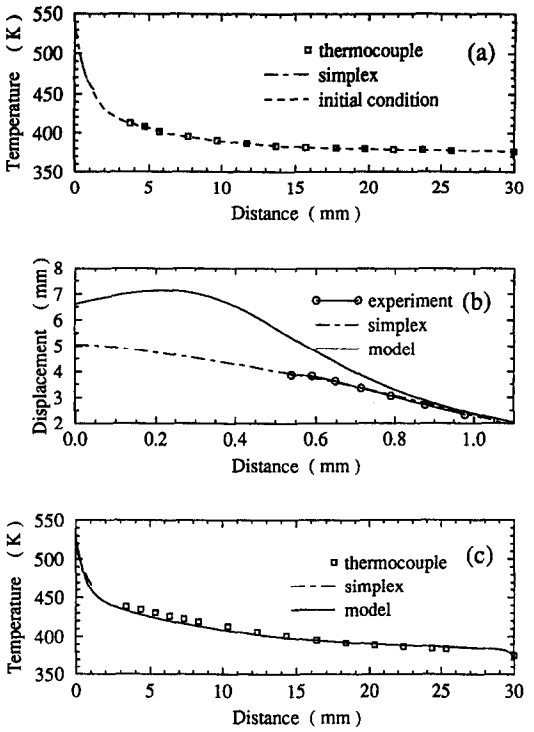

FIG. 6. Results of experiment E3. The legend is the same as Fig. 4.

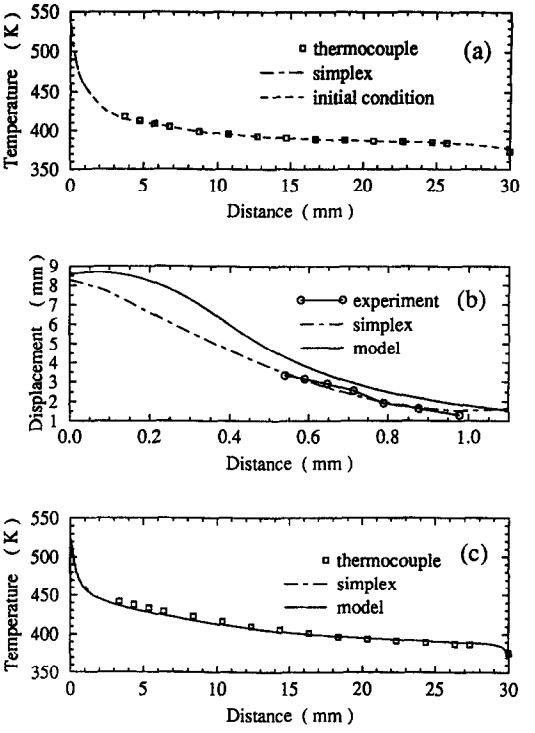

FIG. 8. Results of experiment E5. The legend is the same as Fig. 4.

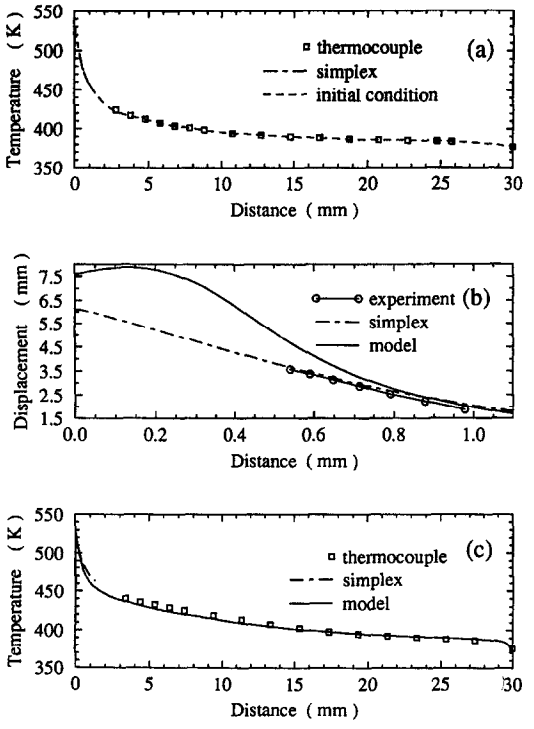

FIG. 7. Results of experiment E4. The legend is the same as Fig. 4.

for $0 \leqslant y \leqslant 1.1$ mm joined to the other one measured by the moving thermocouple with radiation shield for $4 \leqslant y \leqslant 30$ mm. A second-order temperature polynomial function $T(y)$ allows us to join the two profiles. As the temperature field has been modified the velocity profile is corrected, as below, in order to ensure mass flow rate conservation

$$u(y) = \frac{\rho^*(y)\, u^*(y)}{\rho(y)}, \tag{21}$$

where u^* and ρ^* are related to the initial calculation. At section 2 we compare the wall conductive flux in the gas determined by the turbulence model, called ϕ_{2m}, with the one deduced from the laser beam displacements, called ϕ_{2d}. However, the five following

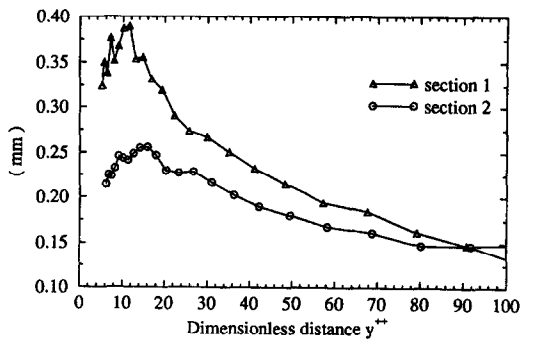

FIG. 9. Standard deviation fields of laser beam displacement vs y^{++} at sections 1 and 2.

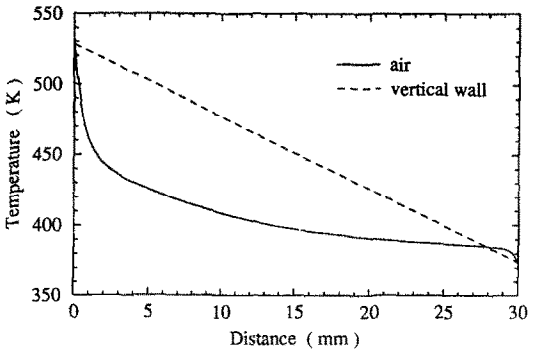

FIG. 10. Comparison between the temperature fields in air in a central region and in a vertical wall for experiment E3 at section 1 vs the distance y to the upper wall.

effects must be considered in order to correct the value of ϕ_{2m}:

1. The upper plate temperature T_u is not rigorously uniform. It is about ΔT_u lower at section 2 than the mean value introduced in the turbulence model. The wall conductive flux ϕ_{2m} in the gas is equal to $h(T_u - T_{b2})$, where h is the convective heat transfer coefficient and T_{b2} is the bulk temperature determined by the turbulence model at section 2. If we assume that T_{b2} is not affected by small variations of T_u the relative error on ϕ_{2m} is then

$$\left(\frac{\Delta\phi_{2m}}{\phi_{2m}}\right)_{\mathrm{I}} = \frac{\Delta h}{h} + \frac{\Delta T_u}{T_u - T_{b2}}. \tag{22}$$

The relative variation of h has been studied numerically. For a variation of 10 K in T_b $\Delta h/h$ is equal to about 4×10^{-3}, which is neglected in equation (22).

2. The uncertainty on the temperature at section 1 measured by the thermocouple 4 mm away from the walls is ± 1.5 K. We obtain therefore a second source of error

$$\left(\frac{\Delta\phi_{2m}}{\phi_{2m}}\right)_{\mathrm{II}} = \frac{-\Delta T_{b2}}{T_u - T_{b2}}. \tag{23}$$

If we assume that h is constant between sections 1 and 2, then we have $\Delta T_{b2} = \Delta T_{b1}$ and we obtain finally

$$\left(\frac{\Delta\phi_{2m}}{\phi_{2m}}\right)_{\mathrm{II}} = \frac{-\Delta T_{b1}}{T_u - T_{b2}}. \tag{24}$$

3. The flow in the wind channel is not exactly bi-dimensional. The two vertical walls are not isolated but are characterized in a section by a quasi-linear temperature profile between T_u and T_l (Fig. 10). Then we must take into account the heating effect of the gas by these lateral plates along the channel on the wall conductive flux at section 2. The heat flux transfered from the vertical walls to the gas can be evaluated from Fig. 10 by assuming that the convective heat transfer coefficient h is the same as on the upper wall. This effect leads to an increase in the air enthalpy and bulk temperature at section 2, represented as ΔH_2 and ΔT_{b2}, respectively. Then the relative decrease in the flux ϕ_{2m} is

$$\left(\frac{\Delta\phi_{2m}}{\phi_{2m}}\right)_{\mathrm{III}} = \frac{-\Delta T_{b2}}{T_u - T_{b2}} = \frac{-\Delta H_2}{(H_2 - H_1)} \frac{(T_{b2} - T_{b1})}{(T_u - T_{b2})}, \tag{25}$$

where H_1 and H_2 are the air enthalpies at section 1 and 2, respectively.

4. The uncertainty on the measurement of the mass flow rate $\dot{m}$ is about $\pm 1\%$. The change in the heat flux at section 2 is deduced from a balance of enthalpy between two sections of the wind channel at x and $x + \mathrm{d}x$ if we assume the same constant value of h for the upper and the lower walls between section 1 and 2. We obtain after integration between section 1 and 2

$$\frac{T_u + T_l - 2T_{b2}}{T_u + T_l - 2T_{b1}} = \exp\left[\frac{-2L_1 h}{\dot{m} c_p}(x_2 - x_1)\right], \tag{26}$$

where c_p is the heat capacity. The relative error on the wall conductive flux is then

$$\left(\frac{\Delta\phi_{2m}}{\phi_{2m}}\right)_{\mathrm{IV}} = \frac{\Delta\dot{m}}{\dot{m}}\left[0.8 + \frac{0.2hL_1}{\dot{m}c_p}\left(\frac{T_u + T_l - 2T_{b2}}{T_u - T_{b2}}\right)\right]. \tag{27}$$

5. The experimental set-up does not allow for the measurement of the thermal turbulence intensity $(\overline{T'^2})^{1/2}/\bar{T}$ at the inlet of the channel. The effect of this

Table 4. Relative errors on the wall conductive flux ϕ_{2m} determined by the 2D turbulence model

Experiment	ΔT_u [K]	ΔT_{b2} [K]	$\frac{\Delta H_2}{H_2 - H_1}$ [%]	$\left(\frac{\Delta\phi_{2m}}{\phi_{2m}}\right)_{\mathrm{I}}$ [%]	$\left(\frac{\Delta\phi_{2m}}{\phi_{2m}}\right)_{\mathrm{II}}$ [%]	$\left(\frac{\Delta\phi_{2m}}{\phi_{2m}}\right)_{\mathrm{III}}$ [%]	$\left(\frac{\Delta\phi_{2m}}{\phi_{2m}}\right)_{\mathrm{IV}}$ [%]	$\left(\frac{\Delta\phi_{2m}}{\phi_{2m}}\right)_{T}$ [%]
E1	-3	± 1.5	$+17.3$	-2.4	± 1.1	-2.1	± 0.8	-4.5 ± 1.9
E2	-3	± 1.5	$+18.9$	-2.4	± 1.1	-2.2	± 0.8	-4.6 ± 1.9
E3	-10	± 1.5	$+19.8$	-8.0	± 1.1	-2.2	± 0.8	-10.2 ± 1.9
E4	-7	± 1.5	$+23.6$	-5.8	± 1.1	-2.3	± 0.8	-8.1 ± 1.9
E5	-9	± 1.5	$+20.2$	-7.4	± 1.1	-1.9	± 0.8	-9.3 ± 1.9

H_1 and H_2 are, respectively, the air enthalpies at sections 1 and 2. T_{b2} is the bulk temperature of the model at section 2.

Table 5. Comparison between the experimental wall conductive flux ϕ_{2d} and the flux predicted by the model ϕ_{2m} before and after corrections

Experiment	ϕ_{2m} [kW m^{-2}]	ϕ_{2m} (corrected) [kW m^{-2}]	$(dT/dy)_{2d}$ [K mm^{-2}]	ϕ_{2d} [kW m^{-2}]
E1	1.88	1.79±0.03	31.4± 1.4	1.35±0.06
E2	2.79	2.66±0.05	63.0± 3.7	2.71±0.16
E3	3.77	3.38±0.06	69.3± 9.1	2.98±0.39
E4	4.24	3.89±0.07	93.5± 3.8	4.02±0.16
E5	4.73	4.30±0.08	115.1±16.3	4.95±0.70

phenomenon on ϕ_{2m} the wall conductive heat flux at section 2, has been numerically studied; ϕ_{2m} is increased by about 2.3% when taking an initial thermal turbulence intensity of 0.15 which is a large overestimation of the value reached in our experimental conditions. We have thus neglected this effect in the following.

The total relative error is equal to the sum of the previous errors (1) to (4). All these effects are summarized in Table 4. The wall conductive flux determined by the 2D turbulence model ϕ_{2m} is compared in Table 5 to the one deduced from the laser beam deflection ϕ_{2d}. This last flux agrees with ϕ_{2m} for experiments E2–E5 when taking into account the uncertainties on each term. However, the model leads to a value 25% larger than that deduced from the deflection technique in the case of experiment E1 characterized by a Reynolds number close to 10^4. In fact, even for an isothermal medium, there are discrepancies of about 23% between the predictions of the skin-friction coefficient from different turbulence models [31]. This quantity is similar to the Nusselt number considered here. Discrepancies related to other thermal quantities have also been observed [26]. The models differ in values of constants, C_λ in particular, or in the kind of boundary conditions, related to ε and ε_θ for example. On the other hand the model in use here agrees with the experiments of Fulachier *et al.* [7] and Blom [9] characterized by Reynolds numbers based on the boundary layer thickness equal to 3.8×10^4 and 1.9×10^4, respectively [26]. Consequently it is difficult to conclude as regards the experimental and theoretical discrepancies observed between experiment E1 and our model, for Re_{Dh} close to 10^4.

The air temperature values measured by the movable thermocouple in the region $4 < y < 26$ mm are close to those deduced from the turbulence model (Figs. 4c–8c).

REFERENCES

1. W. Hauf and U. Grigull, Optical methods in heat transfer. In *Advances in Heat Transfer*, Vol. 6, p. 133. Academic Press, New York (1970).
2. Y. Iritani, N. Kasagi and M. Hirata, Heat transfer mechanism and associated turbulence structure in the near-wall region of a turbulent boundary layer. In *Turbulent Shear Flows* (Edited by L. J. S. Bradbury, F. Durst, B. E. Launder, F. W. Schmidt and J. H. Whitelaw), Vol. 4, pp. 223–234. Springer, Berlin (1985).
3. L. V. Krishnamoorthy and R. A. Antonia, Temperature dissipation measurements in a turbulent boundary layer. *J. Fluid Mech.* **176,** 265–281 (1987).
4. M. Hishida and Y. Nagano, Simultaneous measurements of velocity and temperature in nonisothermal flows. *J. Heat Transfer* **100,** 340–345 (1978).
5. J. Hoch and L. M. Jiji, Theoretical and experimental temperature distribution in two dimensional turbulent jet-boundary interaction. *J. Heat Transfer* **103,** 331–336 (1981).
6. A. Soufiani and J. Taine, High-resolution spectroscopy temperature measurements in laminar channel flows. *Appl. Opt.* **27,** 3754–3760 (1988).
7. L. Fulachier, E. Verollet and I. Dekeyser, Résultats expérimentaux concernant une couche limite turbulente avec aspiration et chauffage à la paroi. *Int. J. Heat Mass Transfer* **20,** 731–739 (1977).
8. R. A. Antonia, L. V. Krishnamoorthy and L. Fulachier, Correlation between the longitudinal velocity fluctuation and temperature fluctuation in the near wall region of a turbulent boundary layer. *Int. J. Heat Mass Transfer* **31,** 723–730 (1988).
9. J. Blom, Experimental determination of the turbulent Prandtl number in a developing temperature boundary layer. *4th Int. Heat Transfer Conf.*, Versailles, Paris, Vol. 2 (1970).
10. V. Motevalli, C. H. Marks and B. J. McCaffrey, Cross-correlation velocimetry for measurement of velocity and temperature profiles in low-speed turbulent non-isothermal flows. *J. Heat Transfer* **114,** 331–337 (1992).
11. A. Y. Chang, E. C. Rea and R. K. Hanson, Temperature measurements in shock tubes using a laser-based absorption technique. *Appl. Opt.* **26,** 885–893 (1987).
12. F. Kritzstein, Etude théorique et expérimentale des effets de la turbulence sur le rayonnement infrarouge des gaz. Application à un écoulement turbulent dans un canal. Thesis, Ecole Centrale Paris (1993).
13. D. Stepowski and G. Cabot, Single-shot temperature and mixture fraction profiles by Rayleigh scattering in the development zone of a turbulent diffusion flame. *Combust. Flame* **88,** 296–308 (1992).
14. B. Attal, S. Druet, R. Bailly, M. Péalat and J. P. Taran, Techniques Raman d'études des écoulements et des flammes par laser. *SPECTRA* 2000 **7,** 37–46 (1979).
15. R. J. Hall, CARS spectra of combustion gases. *Combust. Flame* **35,** 47–60 (1979).
16. R. J. Goldstein, Interferometer for aerodynamic and heat transfer measurements. *Rev. Sci. Instr.* **36,** 1408–1410 (1965).
17. F. Mayinger and A. Chavez, Measurement of direct-contact condensation of pure saturated vapour on an injection spray by applying pulsed laser holography. *Int. J. Heat Mass Transfer* **35,** 691–702 (1992).
18. R. J. Goldstein, Optical measurement of temperature. In *Measurement Techniques in Heat Transfer* (Edited by E. R. G. Eckert and R. J. Goldstein), AGARD, NATO Report, No. 130, pp. 177–228 (1970).
19. J. C. Mombo-Caristan, L. C. Philippe, M. Y. Perrin and J. P. Martin, Laser beam deviation as a local density

probe. Application to supersonic free jets. *Experiments in Fluids* **7**, 303–308 (1989).
20. G. Rousset and F. Lepoutre, Mesures de diffusivités thermiques par la méthode photoacoustique et par l'effet mirage. *Revue Phys. Appl.* **17**, 201–207 (1982).
21. M. A. Olmstead, N. M. Amer, S. Kohn, D. Fournier and A. C. Boccara, Photothermal displacement spectroscopy: an optical probe for solids and surfaces. *Appl. Phys.* **A32**, 141–154 (1983).
22. W. B. Jackson, N. M. Amer, A. C. Boccara and D. Fournier, Photothermal deflection spectroscopy and detection. *Appl. Opt.* **20**, 1334–1344 (1981).
23. L. Zhang, J. P. Petit and J. Taine, Measurements of temperature profiles in gases by laser beam deflection. *Revue Phys. Appl.* **24**, 401–410 (1989).
24. A. Soufiani, Etudes théoriques et expérimentales des transferts couplés par convection laminaire ou turbulente et rayonnement dans un milieu gazeux à température élevée. Thesis, Université Paris XI, Orsay (1987).
25. A. Soufiani and J. Taine, Experimental and theoretical studies of combined radiative and convective transfer in CO_2 and H_2O laminar flows. *Int. J. Heat Mass Transfer* **32**, 477–486 (1989).
26. P. Mignon, Etude théorique du couplage convection turbulente-rayonnement dans un écoulement de gas dans un canal. Thermodégradation de la paroi. Thesis, Ecole Centrale Paris (1992).
27. A. Soufiani, P. Mignon and J. Taine, Radiation effects on turbulent heat transfer in channel flows of infrared active gases. In *Radiation Heat Transfer: Fundamentals and Applications* (Edited by Smith *et al.*), HTD-137, pp. 141–148. ASME, New York (1990).
28. M. Born and E. Wolf, *Principles of Optics*. Pergamon Press, Oxford (1975).
29. G. S. G. Beveridge and R. S. Schechter, *Optimization: Theory and Practice*. McGraw-Hill, New York (1970).
30. W. Spendly, G. R. Hext and F. H. Himsworth, *Technometrics* **4**, 441–449 (1962).
31. V. C. Patel, W. Rodi and G. Scheuerer, Turbulence models for near-wall and low Reynolds number flows: a review. *AIAA J.* **23**, 1308–1319 (1985).
32. W. P. Jones, B. E. Launder and I. Dekeyser, The prediction of laminarization with a two-equation model of turbulence. *Int. J. Heat Mass Transfer* **15**, 301–314 (1972).
33. C. K. G. Lam and K. A. Bremhorst, A modified form of the k–ε model for predicting wall turbulence. *J. Fluid. Engng* **103**, 456–460 (1981).

APPENDIX

The turbulence model used comes from a k–ε model, initially introduced by Jones *et al.* [32] and modified by Lam and Bremhorst [33] by introducing wall damping functions. This approach has been extended in the EM2C laboratory to variable thermophysical properties by Soufiani [24] and to the transport of thermal turbulent quantities, the temperature variance and its dissipation rate, by Mignon *et al.* [26, 27]. The boundary layer hypothesis (i.e. neglecting the second derivatives in the streamwise direction) is assumed. All time-averaged transport equations of the turbulence model can be put in a steady-state case into the form

$$c\frac{\partial(\rho u\phi)}{\partial x}+c\frac{\partial(\rho v\phi)}{\partial y}=\frac{\partial}{\partial y}\left[\Gamma_\phi\frac{\partial\phi}{\partial y}\right]+S_\phi,$$

where the parameters c, ϕ, Γ_ϕ and S_ϕ are given in Table A1.

Table A1. Parameters of the 2D turbulence balance equations

Equation	c	ϕ	Γ_ϕ	S_ϕ
Continuity	1	1	0	0
Momentum	1	u	$\bar{\mu}+\mu_t$	$-\dfrac{\partial\bar{p}}{\partial x}$
Energy	$\bar{c}_p$	$\tilde{T}$	$\bar{\lambda}+\lambda_t$	$-\tilde{u}\dfrac{\partial\bar{p}}{\partial x}+(\bar{\mu}+\mu_t)\left(\dfrac{\partial\tilde{u}}{\partial y}\right)^2$
Turbulent kinetic energy	1	k	$\bar{\mu}+\dfrac{\mu_t}{\sigma_k}$	$\mu_t\left(\dfrac{\partial\tilde{u}}{\partial y}\right)^2-\bar{\rho}\varepsilon$
Dissipation rate of k	1	ε	$\bar{\mu}+\dfrac{\mu_t}{\sigma_\varepsilon}$	$C_{\varepsilon_1}f_1\dfrac{\varepsilon}{k}\mu_t\left(\dfrac{\partial\tilde{u}}{\partial y}\right)^2-C_{\varepsilon_2}f_2\dfrac{\varepsilon^2}{k}$
Half-variance of T	$\bar{c}_p$	θ	$\bar{\lambda}+\dfrac{\lambda_t}{\sigma_\theta}$	$\lambda_t\left(\dfrac{\partial\tilde{T}}{\partial y}\right)^2-\bar{\rho}\bar{c}_p\varepsilon_\theta$
Dissipation rate of θ	$\bar{c}_p$	ε_θ	$\bar{\lambda}+\dfrac{\lambda_t}{\sigma_{\varepsilon_\theta}}$	$c_{P1}f_{P1}\dfrac{\varepsilon_\theta}{k}\bar{c}_p\mu_t\left(\dfrac{\partial\tilde{u}}{\partial y}\right)^2+C_{P2}f_{P2}\lambda_t\dfrac{\varepsilon_\theta}{\theta}\left(\dfrac{\partial\tilde{T}}{\partial y}\right)^2$ $-\bar{\rho}\bar{c}_p\left(C_{D1}f_{D1}\dfrac{\varepsilon\varepsilon_\theta}{k}+C_{D2}f_{D2}\dfrac{\varepsilon_\theta^2}{\theta}\right)$

Table A2. Turbulence model constants

σ_k	σ_ε	σ_θ	$\sigma_{\varepsilon\theta}$	C_μ	$C_{\varepsilon1}$	$C_{\varepsilon2}$	C_λ	C_{P1}	C_{P2}	C_{D1}	C_{D2}
1	1.3	1	1	0.09	1.44	1.92	0.14	0.9	0.72	1.1	0.8

The turbulent viscosity μ_t and conductivity λ_t are classically modelled by

$$\mu_t = \bar{\rho} C_\mu f_\mu \frac{k^2}{\varepsilon}, \quad \lambda_t = \bar{\rho}\,\bar{c}_p\, C_\lambda f_\lambda k \sqrt{\frac{k}{\varepsilon}\frac{\theta}{\varepsilon_\theta}}.$$

The wall damping functions are [26, 27]

$$f_\mu = (1-\exp(-0.0165R_y))^2\left(1+\frac{20.5}{R_T}\right)$$

$$f_\mu = (1-\exp(-0.0165R_y)) \times (1-\exp(-0.0165Pr\,R_y))\left(1+\frac{20.5}{R_{M,T}}\right)$$

$$f_1 = 1+\left(\frac{0.05}{f_\mu}\right)^2, \quad f_2 = 1-\exp(-R_T^2)$$

$$f_{P1} = f_{P2} = 1+\left(\frac{0.05}{f_\lambda}\right)^3,$$

$$f_{D1} = f_{D2} = 1-\exp(-R_{M,T}^2),$$

where R_T, R_y and $R_{M,T}$ are different Reynolds numbers defined by

$$R_T = \frac{\bar{\rho}k^2}{\bar{\mu}\varepsilon}, \quad R_y = \frac{\bar{\rho}\sqrt{k}}{\bar{\mu}}y,$$

$$R_{M,T} = \sqrt{\left(\frac{\bar{\rho}k^2}{\bar{\mu}\varepsilon}\right)\left(\frac{\bar{\rho}\bar{c}_p k\theta}{\bar{\lambda}\varepsilon_\theta}\right)}.$$

The model constants are summarized in Table A2. The boundary conditions at the walls are characterized by zero values for u, v, k, $\partial\varepsilon/\partial y$, θ and $\partial\varepsilon_\theta/\partial y$. The thermal conditions are characterized by the imposed values T_u and T_l of the upper and lower wall temperature, respectively.